Climate Dynamics (2000) 16:451–467 

G. M. Flato · G. J. Boer · W. G. Lee
N. A. McFarlane · D. Ramsden · M. C. Reader
A. J. Weaver

# The Canadian Centre for Climate Modelling and Analysis global coupled model and its climate

Received: 24 September 1998 / Accepted: 8 October 1999

**Abstract** A global, three-dimensional climate model, developed by coupling the CCCma second-generation atmospheric general circulation model (GCM2) to a version of the GFDL modular ocean model (MOM1), forms the basis for extended simulations of past, current and projected future climate. The spin-up and coupling procedures are described, as is the resulting climate based on a 200 year model simulation with constant atmospheric composition and external forcing. The simulated climate is systematically compared to available observations in terms of mean climate quantities and their spatial patterns, temporal variability, and regional behavior. Such comparison demonstrates a generally successful reproduction of the broad features of mean climate quantities, albeit with local discrepancies. Variability is generally well-simulated over land, but somewhat underestimated in the tropical ocean and the extratropical storm-track regions. The modelled climate state shows only small trends, indicating a reasonable level of balance at the surface, which is achieved in part by the use of heat and freshwater flux adjustments. The control simulation provides a basis against which to compare simulated climate change due to historical and projected greenhouse gas and aerosol forcing as described in companion publications.

G. M. Flato (✉) · G. J. Boer · W. G. Lee · N. A. McFarlane
D. Ramsden · M. C. Reader
Canadian Centre for Climate Modelling
and Analysis Atmospheric Environment Service,
University of Victoria, British Columbia, Canada
E-mail: greg.flato@ec.gc.ca

A. J. Weaver
School of Earth and Ocean Sciences,
University of Victoria, BC, Canada

## 1 Introduction

Potential anthropogenic influence on global climate has spurred development of models capable of reproducing contemporary mean climate and its variability, and of exploring scenarios of future climate change. Such models involve realistic representation of the major components of the climate system and their interaction. In particular, simulating the transient evolution of the climate system requires that the full three-dimensional circulation of both the atmosphere and ocean are represented so as to include the ocean's role in sequestering and redistributing heat and freshwater over a range of time scales, and in supporting coupled modes of climate variability.

The model discussed represents a continuation in the development of global climate models at the Canadian Centre for Climate Modelling and Analysis (CCCma). Previous models have focused on the atmosphere with either specified ocean temperatures or a 50 m mixed-layer ocean (Boer et al. 1984, 1992; McFarlane et al. 1992, hereafter referred to as MBBL). The present model, termed CGCM1, is the first version to include a complete three-dimensional ocean component. This model is intended for use in long (multi-century) climate experiments, and its resolution (T32L10 atmosphere and 1.86°L29 ocean) is similar to other coupled models of this type as summarized for instance by Gates et al. (1996), and more recently in the Coupled Model Intercomparison Project (http://www-pcmdi.llnl.gov/cmip/). This model also uses monthly flux adjustments for both heat and freshwater. Although several coupled models are now able to produce reasonably drift-free control climates without them, roughly half of the coupled models currently in use still employ flux adjustments.

We describe the model, focusing primarily on the new aspects which arise on coupling with a three-dimensional ocean. We then examine results from a 200 year control simulation, and assess, in a systematic manner, the ability of the model to reproduce contemporary climate

in terms of its mean, its variability, and its regional behavior, primarily in terms of surface quantities. In two companion papers, Boer et al. (2000a, b) discuss the results obtained using this model to simulate the climatic response to an imposed scenario of increasing greenhouse gases and aerosols.

## 2 Atmosphere, sea-ice, and inland seas

The atmospheric portion of CGCM1 is that described by McFarlane et al. (1992), and is not described in detail here. It is a spectral model with T32 truncation and 10 vertical levels employing a hybrid pressure coordinate discretized in terms of rectangular finite elements. The model uses specific humidity as the moisture variable, has an interactive cloud scheme, moist convection, and a radiative heating formulation based on Fouquart and Bonnel (1980) and Morcrette (1984). A more detailed description of the model, the physical parametrizations employed, and the resulting climate when coupled to a mixed-layer ocean model is provided by MBBL. An analysis of the equilibrium response to doubling $CO_2$ concentration is provided by Boer et al. (1992), and the associate surface energy budget is analyzed in some detail by Boer (1993).

Sea-ice is as described by MBBL, that is, growth and melt is governed by the thermodynamic energy balance and a lead fraction obtained diagnostically through a relationship with sea-ice mass. In the present application, the salt or freshwater flux associated with ice growth or melt is required and is calculated by assuming that salt is immediately expelled upon freezing, leaving pure ice.

The model's surface grid is divided into land, ocean, and inland seas. The grid mask and surface topography are essentially the same as in MBBL with minor changes to accommodate the ocean model grid. The land surface scheme uses a single soil layer with spatially varying field capacity and soil properties. Runoff from the land surface is transferred immediately to the ocean at the outflow point of each prescribed drainage basin. There is no mechanism for subsurface flow or storage and some enclosed drainage basins are arbitrarily connected to the ocean to avoid the possibility of continued accumulation of water on land. Iceberg calving is not explicitly represented and snow accumulates on the ice sheets of Greenland and Antarctica. The resulting net imbalance of freshwater at the ocean's surface is compensated by the flux adjustment described in Sect. 5.

Sub-grid-scale lakes are not explicitly included in the model, however larger 'inland seas' are. These consist of the Baltic, Black, Caspian and Red seas, and are treated as 50 m layers of quiescent seawater, exactly as the mixed-layer ocean in MBBL. An annual cycle of heat flux into the underside of the layer is specified so as to produce sea-surface temperatures and sea-ice seasonal cycles which are close to observations. The water budget of these inland seas is not required to be balanced.

## 3 Ocean model

The ocean model is the GFDL MOM ver. 1 code (Pacanowski et al. 1993) with some modifications. In order to simplify the exchange of fluxes at the surface, both the ocean and atmosphere components of CGCM1 use the same land mask, namely, that of the atmosphere model which, at T32 resolution, has a 'Gaussian transform grid' of $96 \times 48$ grid points. Because many globally-important oceanic processes (e.g. western boundary currents and flow through straits) occur at finer scales, higher resolution in the ocean component is desirable. We use an ocean model grid which has double the resolution of the atmosphere surface grid, with $192 \times 96$ grid points spaced at 1.875° in longitude and 1.856° in latitude. That is, each of the atmosphere's surface grid points is underlain by four ocean grid points. The MOM model avoids the mathematical singularity at the North Pole in a spherical grid by introducing an artificial island, one grid cell in radius. This artificial island only affects the ocean, the sea-ice and atmospheric components of the coupled model span the pole and, over the artificial polar island, use an oceanic heat flux into the ice underside obtained by averaging the surrounding ocean grid points. The ocean grid has 29 vertical levels; the upper four levels are equally-spaced at 50 m, with level spacing increasing below 200 m as shown in Table 1.

Bottom topography is obtained by linear interpolation from the $1° \times 1°$ Gates and Nelson (1975) data set, with a specified minimum ocean depth of 100 m, and the following additional modifications: (1) Denmark Strait is deepened slightly to better resolve overflow of waters formed in the Nordic Seas; (2) the two northernmost row of grid points are assigned constant depths (equal to the zonal mean depth) to suppress topographic instabilities near the pole (Killworth 1987); and (3) Fram Strait is deepened and smoothed, again to suppress topographic instabilities. The resulting topography is smoothed using a 5-point filter, and isolated single grid cell holes in the bottom are filled. Topography north of 66.8°N has this filter applied twice owing to the more stringent stability requirements at higher latitudes.

There are two enclosed ocean basins, Hudson Bay and the Mediterranean Sea, which communicate with the global ocean domain via diffusive mixing across the Hudson and Gibraltar Straits respectively. The same diffusive mixing is applied between Baffin Bay and the Arctic Ocean to approximate unresolved flow through the Canadian Archipelago.

### 3.1 Mixing parameters and sensitivity studies

The ocean model's horizontal and vertical resolution precludes explicit representation of the full range of ocean mixing processes. We parametrize these processes using viscosities and diffusivities specified as follows: the vertical viscosity coefficient is $2 \times 10^{-3}$ m$^2$ s$^{-1}$; the horizontal viscosity is $1.4 \times 10^5$ m$^2$ s$^{-1}$ based on numerical stability requirements; the vertical diffusivity is

**Table 1** Vertical grid spacing in ocean model

| Level | Grid spacing (m) | Depth of grid center (m) |
|---|---|---|
| 1 | 50 | 25.0 |
| 2 | 50 | 75.0 |
| 3 | 50 | 125.0 |
| 4 | 50 | 175.0 |
| 5 | 60 | 230.0 |
| 6 | 70 | 295.0 |
| 7 | 80 | 370.0 |
| 8 | 90 | 455.0 |
| 9 | 105 | 552.5 |
| 10 | 120 | 665.0 |
| 11 | 135 | 792.5 |
| 12 | 150 | 935.0 |
| 13 | 165 | 1092.5 |
| 14 | 180 | 1265.0 |
| 15 | 195 | 1452.5 |
| 16 | 210 | 1655.0 |
| 17 | 225 | 1872.5 |
| 18 | 240 | 2105.0 |
| 19 | 255 | 2352.5 |
| 20 | 270 | 2615.0 |
| 21 | 285 | 2892.5 |
| 22 | 300 | 3185.0 |
| 23 | 300 | 3485.0 |
| 24 | 300 | 3785.0 |
| 25 | 300 | 4085.0 |
| 26 | 300 | 4385.0 |
| 27 | 300 | 4685.0 |
| 28 | 300 | 4985.0 |
| 29 | 300 | 5285.0 |

$3 \times 10^{-5}$ m$^2$ s$^{-1}$, and the horizontal diffusivity is $2 \times 10^3$ m$^2$ s$^{-1}$. To approximate the effect of convection, the vertical momentum and diffusion coefficients are set to 100 m$^2$ s$^{-1}$ when the density profile becomes unstable.

Vertical diffusivity is not strongly tied to numerical stability, and observations provide only a broad range for the vertical diffusion coefficient. The value adopted here was chosen on the basis of previous experience with this model. Experiments by F. Bryan (1987) and later studies, show that the value of vertical diffusivity strongly influences aspects of the ocean circulation like meridional overturning. In order to assess the impact of our particular choice of diffusivity on various features of the ocean circulation, we conduct a suite of sensitivity studies with a version of the model which differs from that described already by having double the longitudinal grid spacing (i.e. 1.86° × 3.75° latitude/longitude). In all of these experiments, annual mean wind stress from the Hellerman and Rosenstein (1983) climatology is used, along with restoring of surface temperature and salinity to the climatological annual means of Levitus (1982), with 30 day relaxation time constants (see also Weaver and Hughes 1996, for a more detailed description of this version of the model and its boundary conditions).

Six experiments are conducted: four with constant vertical diffusivities ($1 \times 10^{-4}$, $5 \times 10^{-5}$, $3 \times 10^{-5}$, and $2 \times 10^{-5}$ m$^2$ s$^{-1}$), and two with vertical profiles of diffusivity, $K_v$, given by

$$K_v = A_o + \frac{C_r}{\pi} \tan^{-1}(S(z - z_o)) \ . \quad (1)$$

Two versions of Eq. (1) are used. The first follows Bryan and Lewis (1979) with $A_o$, $C_r$, $S$, and $z_o$ taken to be $8 \times 10^{-5}$ m$^2$ s$^{-1}$, $1.05 \times 10^{-4}$ m$^2$ s$^{-1}$, $4.5 \times 10^{-3}$ m$^{-1}$, and 2500 m, respectively; the second follows Cummins (1991) with values of $1.39 \times 10^{-4}$ m$^2$ s$^{-1}$, $2.51 \times 10^{-4}$ m$^2$ s$^{-1}$, $5 \times 10^{-3}$ m$^{-1}$, and 1000 m, respectively. All of the experiments are run to near equilibrium (between 1750 and 2500 years).

The results of the six experiments are shown in Table 2, in which several climatically important ocean circulation quantities are compared. These include two measures of the meridional overturning circulation in the Atlantic at 24°N, the northward heat transport in both the Atlantic and Pacific at 24°N, and the barotropic transport through the Indonesian Archipelago and Drake Passage. Observational estimates, admittedly crude, are provided in the last row of the table. The meridional circulation in the Atlantic consists of two cells, an upper cell with northward-flowing thermocline water and southward flowing intermediate and deep water, underlain by reversed cell whose northward-flowing component represents inflow of Antarctic Bottom Water (AABW). The strength of these two cells in the model at 24°N can be compared to the thermocline and bottom water transports estimated by Schmitz and McCartney (1993, their Table 2). The low-resolution model results all indicate an Atlantic overturning circulation which is too weak compared to the observational estimates, although it should be noted that the maximum in the overturning streamfunction, which occurs further north, is about 50% higher in the model than the tabulated values at 24°N.

Heat transport turns out to be less sensitive, spanning a range of less than 20% for a five-fold increase in $K_v$. Interestingly, the heat transport in the Pacific is a maximum near $K_v = 3 \times 10^{-5}$ m$^2$ s$^{-1}$, whereas the heat transport in the Atlantic increases monotonically with $K_v$ over the range explored. However, according to the hydrographic estimates of Bryden et al. (1991), the model underestimates the oceanic heat transport at 24°N for all our choices of $K_v$. This may be due to poor resolution of western boundary currents according to Fanning and Weaver (1997).

These sensitivity results indicate that, although the meridional and horizontal mass transports in the model respond to changes in the value of vertical diffusivity, the poleward heat transports are rather insensitive. Given the importance of oceanic heat transports in the coupled climate system, it is reassuring that uncertainty in the value of vertical diffusivity has a modest impact.

Two additional rows in Table 2, labelled 'high-resolution spin-up' and 'coupled model', allow a comparison of the various ocean circulation quantities obtained from the equilibrium spin-up (at the full 1.86° resolution, using AGCM winds rather than observed climatology), and averaged over the coupled control run respectively. Comparison of the high-res spin-up results to the $K_v = 3 \times 10^{-5}$ m$^2$ s$^{-1}$ results illustrates the combined effect of higher resolution and AGCM mean wind stress. The most noticeable differences are the increase strength of the north Atlantic overturning circulation and a weakening of the Antarctic circumpolar current. Results from the coupled model are discussed in more detail in Sect. 6.4.

## 4 Coupling scheme

The atmosphere and ocean components communicate once per day by exchanging daily average quantities as illustrated schematically in Fig. 1. Daily averaged fluxes of heat and freshwater at the ocean surface are computed by the atmosphere component and a seasonally varying flux adjustment is applied (see Sect. 5). These 'adjusted' fluxes, together with unadjusted momentum flux components, are used to drive the ocean component for one day. In turn, the ocean component provides a daily averaged sea-surface temperature which is subsequently modified by a monthly mean temperature adjustment, and returned to the atmosphere component for the next day. The atmospheric model linearly interpolates between the daily 'target' ocean temperature and the previous day's temperature to get surface ocean temperature at each time step. To

**Table 2** Results of vertical diffusivity sensitivity study

| Experiment | Maximum Atlantic overturning at 24°N (Sv) | Northward bottom-water transport in the Atlantic at 24°N (Sv) | Northward Pacific heat transport at 24°N (PW) | Northward Atlantic heat transport at 24°N (PW) | Indonesian through-flow (Sv) | Drake Passage transport (Sv) |
|---|---|---|---|---|---|---|
| $K_v = 1 \times 10^{-4}$ m$^2$ s$^{-1}$ | 11.0 | 4.3 | 0.37 | 0.67 | 22.1 | 180.3 |
| $K_v = 5 \times 10^{-5}$ m$^2$ s$^{-1}$ | 9.3 | 2.8 | 0.42 | 0.61 | 18.7 | 145.7 |
| $K_v = 3 \times 10^{-5}$ m$^2$ s$^{-1}$ | 8.5 | 2.3 | 0.44 | 0.59 | 17.2 | 132.2 |
| $K_v = 2 \times 10^{-5}$ m$^2$ s$^{-1}$ | 8.2 | 2.1 | 0.43 | 0.58 | 16.4 | 125.2 |
| Bryan and Lewis | 8.2 | 4.1 | 0.37 | 0.54 | 17.1 | 131.5 |
| Cummins | 7.7 | 4.9 | 0.45 | 0.58 | 22.3 | 165.3 |
| High-resolution spin-up | 14.4 | 3.7 | 0.34 | 0.69 | 16.2 | 112.0 |
| Coupled model | 17.9 | 2.1 | 0.42 | 0.80 | 13.5 | 70.5 |
| "Observed" | 13[a] | 5[a] | 0.76 ± 0.3[b] | 1.22[b] | 10–20[c] | 130–140[d] |

[a] Schmitz and McCartney (1993)
[b] Bryden et al. (1991)
[c] Lukas et al. (1996)
[d] Read and Pollard (1993)

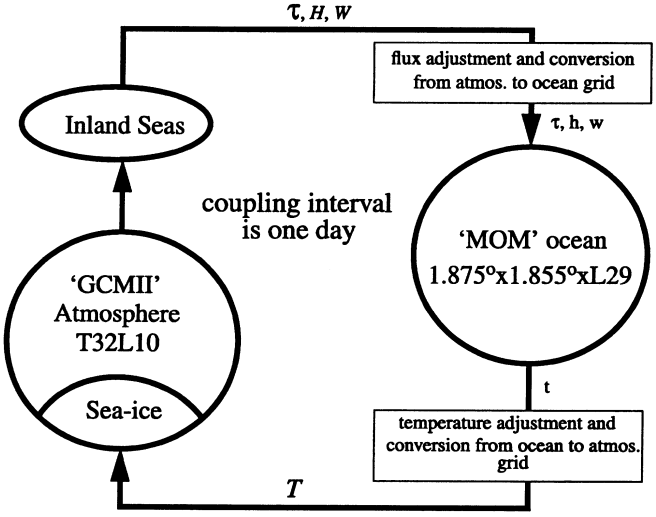


**Fig. 1** Sketch of coupled model components and their interaction

prevent unbounded growth of sea-ice, negative heat flux and temperature adjustments are not allowed if the ice thickness exceeds 2 m. In addition, in the Southern Ocean, the ice cover is required to extract at least 14 W $m^{-2}$ of heat from the ocean surface to prevent continuous accumulation of ice by conversion of snow if temperatures are too cold to allow summer melt.

Because the ocean and atmosphere grids are different, some interpolation or averaging is required when exchanging fluxes or state variables. In the present model this is simplified by the exact 4-to-1 match of the grids, with the ocean and atmosphere land boundaries being coincident. Ocean surface temperatures are averaged, using appropriate area weighting, to produce temperatures on the atmosphere model grid. The momentum flux from an atmospheric grid cell is provided equally to the four ocean grid cells which underlie it, whereas heat and moisture fluxes are partitioned according to the ocean temperature so as to mimic the longwave, sensible and latent heat flux feedbacks which are not resolved at the ocean grid scale.

Symbolically, these exchanges are:

$$\tau = \tau \tag{2}$$

$$h = H + \delta H - \beta(t - T) \tag{3}$$

$$w = W + \delta W - \gamma(t - T) \tag{4}$$

$$T = t + \delta T \tag{5}$$

where $\tau$, $h$, $w$, and $t$ are daily average wind stress, heat flux, moisture flux and temperature respectively, with lower-case characters representing quantities on the high-resolution ocean grid and upper-case characters representing quantities on the low-resolution atmospheric grid. $\delta H$ and $\delta W$ are the mean monthly heat and moisture flux adjustment terms, and $\delta T$ the mean monthly temperature adjustment. The feedback parameters $\beta$ and $\gamma = \beta/L$ are 20 W $m^{-2}$ $K^{-1}$ and $8 \times 10^{-6}$ kg $m^{-2}$ $s^{-1}$ $K^{-1}$, respectively (the heat flux feedback term corresponds to a restoring time of 118 days), and $L$ is the latent heat of vaporization. Note that the average of $t$ over the four ocean grid boxes underlying an atmospheric grid box is equal to $T$, and so the feedback terms in Eqs. (3) and (4) do not alter the total fluxes, but merely redistribute them amongst the four ocean grid boxes.

## 5 Spinup and flux adjustment

High computational cost precludes running the coupled model long enough to reach an 'equilibrium' state and, in fact, there is no guarantee that such an equilibrium would resemble the observed climate. A common procedure therefore (e.g. Sausen et al. 1988) is to run the ocean and atmosphere component models to independent equilibria, constraining the sea-surface temperature and salinity fields to be close to observations, and then to diagnose the mean ocean surface fluxes from both models and apply the difference as a fixed flux adjustment in the coupled model. This flux adjustment procedure is intended to allow the model components to interact freely without introducing large climate drifts which may arise from mismatches between the ocean and atmosphere fluxes. There are a variety of schemes which have been used to derive flux adjustments and, after some trial and error, the following three-step procedure was adopted:

1. Uncoupled equilibrium. The component models are separately integrated to equilibrium which, in the case of the atmospheric component, involved a 20 year simulation. The 20 year average monthly mean fields of wind stress, heat and freshwater flux at the ocean surface were diagnosed from this run. As described in MBBL, this run included coupling to a slab ocean model with a specified heat flux so that the ocean surface temperature, SST, was close to the monthly climatology of Alexander and Mobley (1976). For the ocean component, the spinup used wind stress fields from the atmosphere model and, for heat and salt, restoring boundary conditions with a time scale of 30 days and monthly climatological temperature fields from Alexander and Mobley (1976) and seasonal salinity fields from Levitus (1982). A 30 day time scale was chosen as a compromise between the magnitude of the flux adjustment (which increases with decreasing time scale), and the implied lag in the seasonal cycle (which increases with increasing time scale). During the first 4000 years of this run, the ocean model used asynchronous time-stepping, i.e. momentum and tracer time steps differed by a factor of 48. Over the subsequent 667 years, the time-stepping was made synchronous, such that by year 4667 the ocean was essentially in equilibrium (e.g. the net annual heat and freshwater flux averaged over the global ocean surface were 0.17 W $m^{-2}$ and $-0.29$ mm $d^{-1}$ respectively). Monthly mean fields of heat flux, freshwater flux, and SST were averaged over the last 15 years of this run. The difference between the ocean model SST and the temperature of the slab ocean in the atmospheric model spinup is applied as a 'temperature adjustment' to the ocean temperatures in the coupled model (as indicated in Fig. 1) since the ocean spin-up procedure produces SSTs with a lagged seasonal cycle.

2. Adaptation. The atmosphere and ocean components are coupled and integrated for 14 years using these monthly mean flux adjustment fields, plus a weaker restoring to monthly climatological surface temperature and salinity with a time scale of 60 days. At the end of this 14 year period, the monthly mean heat and freshwater flux adjustments corresponding to these restoring terms were computed and used to modify the original flux adjustments. This 'adaptation' phase allows feedbacks in the coupled system to influence the flux adjustment fields.

3. Additional adjustment. The coupled model is integrated for 5 years using the combined flux adjustments, and any remaining ocean surface salinity drift over the course of this 5 years is diagnosed. A rather slow secular trend in surface salinity was detected, primarily confined to the Arctic Ocean, and likely due to sampling errors in surface runoff. The linear trend in surface salinity was converted into an annual mean freshwater flux adjustment and added to the flux adjustment fields described above.

The resulting annual mean heat and freshwater flux adjustment fields shown in Fig. 2 are comparable to the flux adjustments used in similar coupled models (the annual mean temperature adjustments, not shown, have a magnitude less than 0.5 °C everywhere, except for a very few localized high-latitude maxima where the magnitude may reach 2 °C). The coupled model was run for an additional 70 years to allow some time for coupling transients to dissipate, and the results of a 200 year simulation from this point onward were retained for analysis.

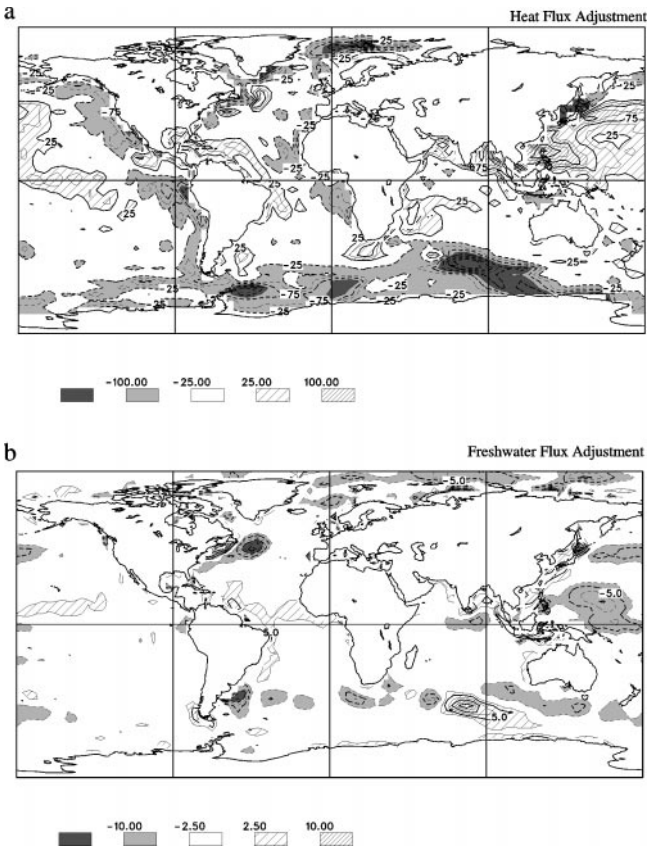


**Fig. 2** **a** Annual mean of heat flux adjustment fields; contour interval is 25 W $m^{-2}$. **b** Annual mean of freshwater flux adjustment fields; contour interval is 2.5 mm $d^{-1}$. In both panels, values are positive when the flux adjustment acts to increase the flux into the ocean. Negative values are *shaded*, while positive values are *hatched*

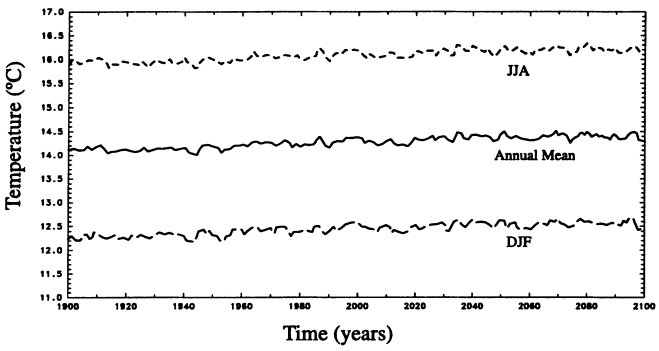


**Fig. 3** Time series of global mean surface air temperature for the 200 year control run. The *solid line* is the annual mean, the *long-dashed line* is the DJF mean, and the *short-dashed line* is the JJA mean

## 6 Control climate

In this section we describe the climate of the coupled model control run. Since the three-dimensional structure of the atmosphere does not differ substantially from that obtained in the mixed-layer ocean version described by MBBL, we focus on the near-surface quantities which are more directly affected by ocean coupling, and on the ocean component of the coupled system.

### 6.1 Surface air temperature

Global mean surface air temperature is a fundamental climate variable and Fig. 3 shows the annual, December–February and June–August (hereafter DJF and JJA respectively) mean time series over a 200 year simulation period. (Note that surface air temperature is an estimate of temperature at the 2 m 'screen height' as described in MBBL). For convenience, when comparing the control simulation to the transient simulation described in the companion papers, all times are measured in years starting at 1900. These time series show that there is a small warming trend in the simulation of less than 0.15 °C per century, which is largely associated with a slow decrease in sea-ice coverage (as will be seen in Sect. 6.5). To put this in perspective, observations (Parker et al. 1995; Jones 1994) over the last 100 years indicate warming at a rate of about 0.6 °C per century, and so the model's climate drift is considerably smaller than the historical trend and certainly much smaller than the projected change due to greenhouse gas and aerosol forcing (e.g. Fig. 1 in Boer et al. 2000b). The modelled DJF and JJA mean temperatures agree remarkably well with values of 12.4 and 15.9 °C respectively from the NCAR climatology (Jenne 1975).

Maps of DJF and JJA surface air temperature, and the difference from observed climatological temperatures (Jenne 1975) are shown in Fig. 4. As in all subsequent figures, the averages are computed using years 1900 to 2100. These temperature patterns closely resemble those described by MBBL as would be expected. Most of the disagreement with observations is over land, particularly areas of high elevation. Reasons for this are given by MBBL along with some discussion of the uncertainty in observed temperatures in these locations. There is comparatively little disagreement in air temperature over the ocean, indicating that the flux adjustment scheme is generally successful. Surface temperature is particularly sensitive to sea-ice cover where large temperature gradients are associated with the transition from a cold ice surface to a relatively warm open ocean. A minor shift in ice cover can therefore cause large temperature differences as can be seen in the Labrador, Greenland and Norwegian Seas in DJF.

Figure 5 shows the interannual standard deviation of seasonal mean surface air temperatures, both modelled and observed. The observations, are based on the land surface air temperature anomaly data of Jones (1994) and the sea-surface temperature data of Parker et al. (1995), as discussed in Nichols et al. (1996) and jointly cited hereafter as JPN. Because the observed climate has warmed over the past century, a linear trend has been removed from the data prior to computing the standard deviation. For consistency the small trend in the model

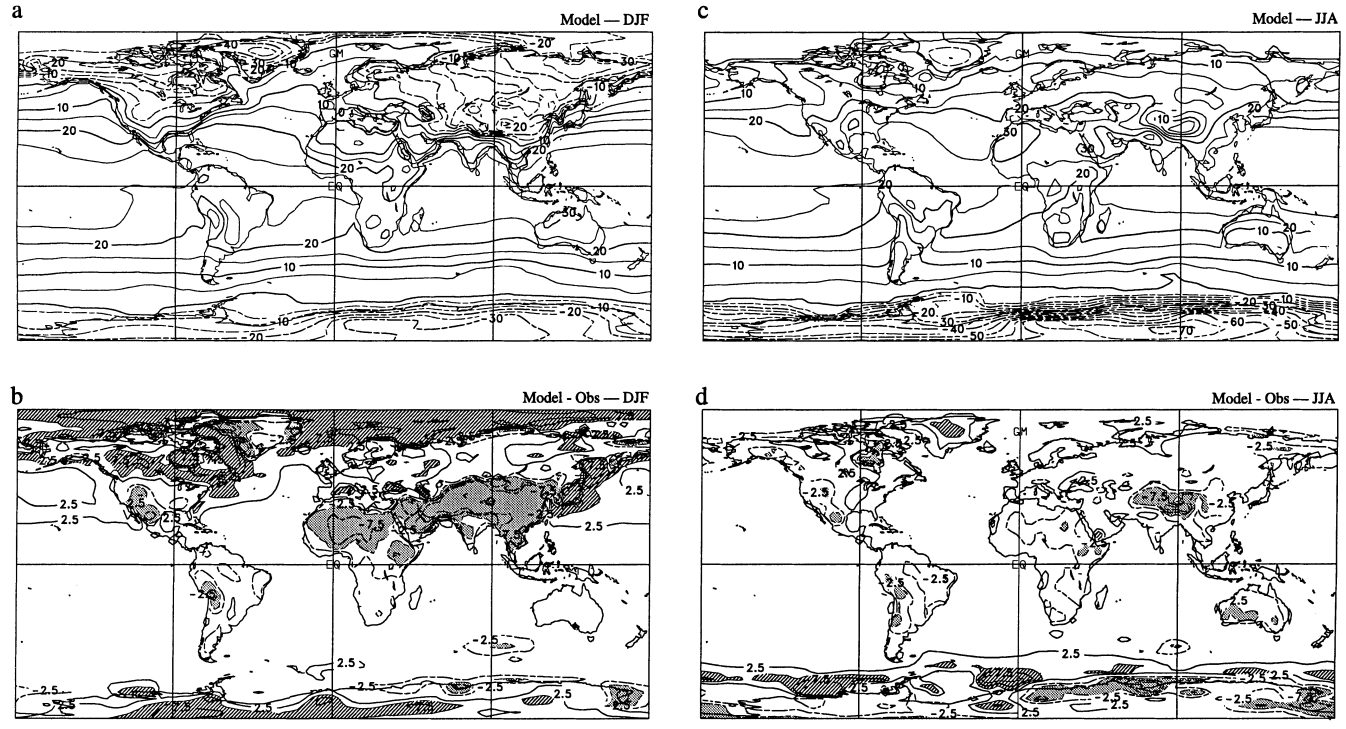


**Fig. 4** **a** Modelled mean DJF surface air temperature. **b** Difference between modelled DJF surface air temperature and NCAR DJF climatology (Jenne 1975). **c** As in **a** but for JJA. **d** as in **b** but for JJA. Contour interval is 5 °C. *Hatching* indicates positive differences greater than 5 °C, whereas *shading* indicates negative differences less than −5 °C

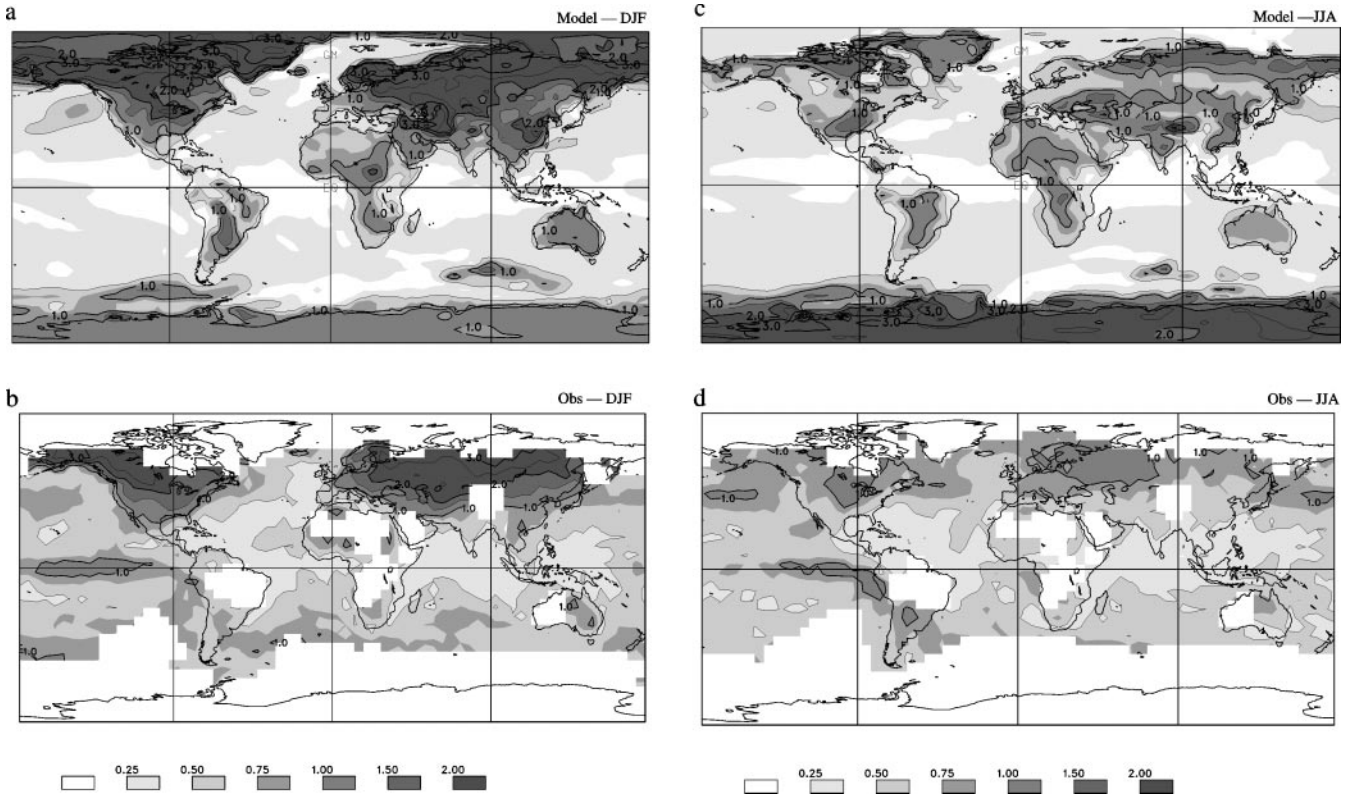


**Fig. 5a–d** Interannual standard deviation of seasonal mean surface air temperature. **a** Modelled, DJF. **b** Observed, DJF. **c** Modelled, JJA. **d** Observed, JJA. See text for details. Contour interval is 0.5 °C. Missing values in observations have been masked

data has likewise been removed for this calculation (although this has a negligible effect). The contrast between land and ocean variability which is clearly visible in the observations is also apparent in the model, presumably owing to the contrast in heat capacity and surface feedback processes. In general the model produces rather realistic variability over land, but tends to underestimate variability over the ocean, particularly in the tropical Pacific and in the boundary current extension regions of the north Pacific and Atlantic. Although sampling and other errors in the observations may contribute to the difference, they are likely not sufficient to explain this difference. In the polar regions, where observations are unfortunately lacking, there is enhanced temperature variability in the winter hemisphere which arises from variability in ice extent and thickness, and variability in ocean convection.

In order to provide a more quantitative comparison, we compare modelled and observed climate in the land-covered portion of the regions shown in Fig. 6. The regions are given special attention in various IPCC reports (e.g. Mitchell et al. (1990). As before, the linear trend has been removed before computing standard deviations. In the modelled time series these linear trends ranged from −0.03 °C per century (south-east Asia in DJF) to +0.2 °C per century (Australia in JJA). The modelled and observed DJF and JJA mean temperatures and interannual standard deviations for each of the regions are given in Tables 3 and 4. The observed mean temperature is from the NCAR climatology (Jenne 1975) and the standard deviation from the JPN temperature anomaly data set. Since the temperature anomaly data are incomplete, we also show in parentheses the value obtained when only the first 96 years of model data are used and masked each year so that model values are only retained if there is a corresponding observed value, the difference is not large. Table entries are shaded where the differences between modelled and observed values are not significantly different at the 5% level (as determined using standard *t*- and *F*-tests for means and standard deviations respectively). The mean temperature comparison in Tables 3 and 4 reinforces features evident in Fig. 4, namely the largest discrepancies are in regions with high topography (e.g. the South East Asia region which includes some of the Tibetan plateau) and a cold bias over desert regions in the cold season (the Sahel in DJF and Australia in JJA). The modelled standard deviations do not differ significantly from the observations in the majority of cases, showing that the model generally reproduces the observed magnitude of variability in these regions.

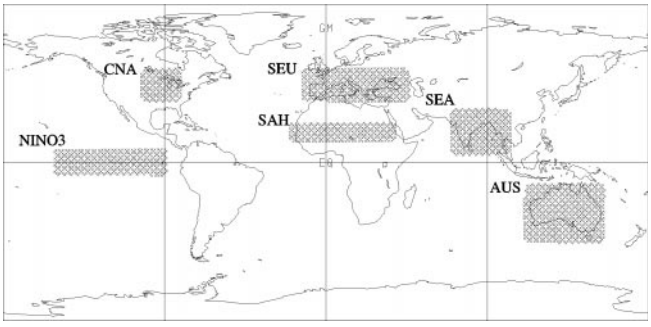


**Fig. 6** Map showing regions selected for analysis of variability over land (comparable to those used in the 1990 IPCC report by Mitchell et al. 1990). These will be referred to in the text as Central North America (*CNA*), Southern Europe (*SEU*), the Sahel (*SAH*), South East Asia (*SEA*) and Australia (*AUS*). In addition, the *NINO3* region is also indicated and will be used to illustrate variability of ocean surface temperature

## 6.2 Mean sea level pressure

The annual cycle of mean sea level pressure in this coupled model control simulation differs little from that described by MBBL, indicating that coupling to a three-dimensional ocean has minor impact on the atmospheric circulation patterns. MBBL also illustrated the atmospheric model's ability to reproduce observed daily variance in surface pressure, i.e. synoptic variability, and so that will not be repeated here. Instead, we compare in Fig. 7, modelled and observed interannual standard deviation of DJF mean surface pressure. This illustrates the model's ability to reproduce lower frequency vari-

**Table 3** DJF land surface air temperature statistics

| Region[a] | Modelled mean (°C) | Observed mean (°C) | Modelled standard deviation (°C) | Observed standard deviation (°C) |
|---|---|---|---|---|
| NAM | −3.7 | −4.20 | 1.65 (1.59) | 1.57 |
| SEA | 10.3 | 18.5 | 0.53 (0.56) | 0.40 |
| SAH | 16.5 | 21.2 | 0.60 (0.58) | 0.66 |
| SEU | 4.7 | 2.81 | 0.61 (0.55) | 0.89 |
| AUS | 27.0 | 27.3 | 0.46 (0.52) | 0.43 |

[a] See caption to Fig. 6 for definitions of the regions. Observations of mean temperature are from the global climatology of Jenne (1975); observations of standard deviation are from the 1900–1995 temperature anomaly data of JPN (see text for details). Values in parentheses indicate model results when only the first 96 years of output are used and masked in such a way as to be consistent with the observations. Shading indicates modelled and observed values whose difference is not statistically significant at the 5% confidence level (based on *t*- and *F*-tests for the mean and standard deviation respectively)

**Table 4** JJA land surface air temperature statistics

| Region | Modelled mean (°C) | Observed mean (°C) | Modelled standard deviation (°C) | Observed standard deviation (°C) |
|---|---|---|---|---|
| NAM | 23.7 | 21.8 | 0.65 (0.59) | 0.91 |
| SEA | 24.4 | 26.5 | 0.30 (0.32) | 0.27 |
| SAH | 27.1 | 30.4 | 0.38 (0.46) | 0.42 |
| SEU | 22.3 | 21.6 | 0.65 (0.69) | 0.41 |
| AUS | 12.4 | 15.6 | 0.48 (0.47) | 0.44 |

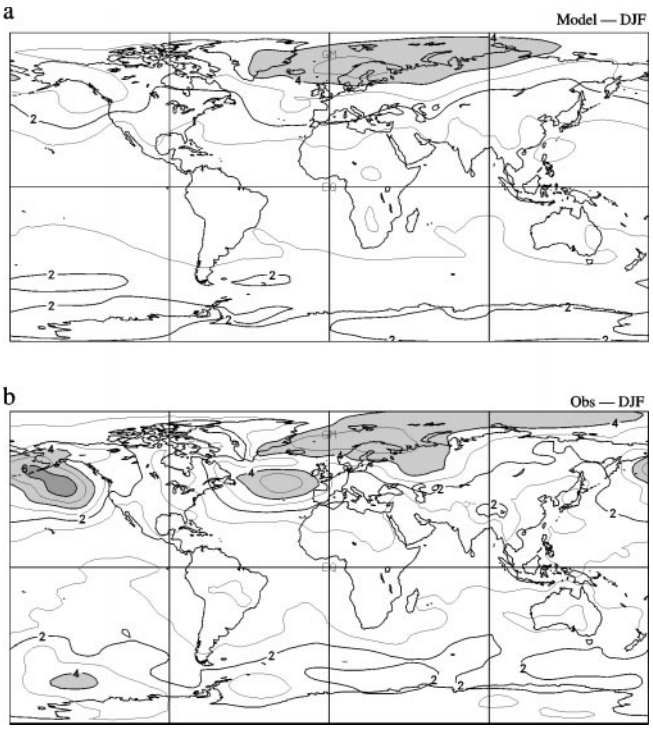


**Fig. 7** **a** Interannual standard deviation of modelled DJF sea level pressure. **b** As in **a** but from ECMWF re-analysis, 1980–1988 (Gibson et al. 1997). Contour interval is 1 hPa

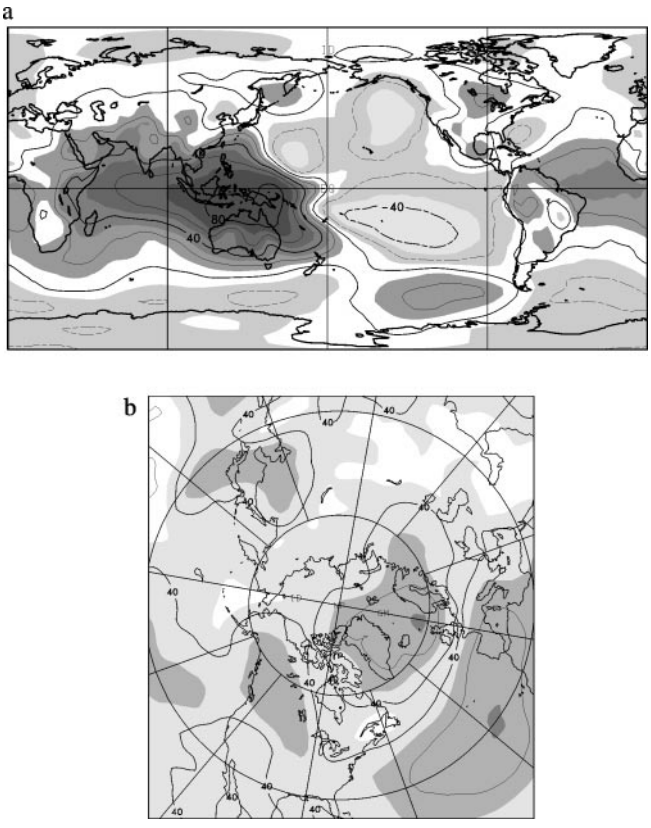


**Fig. 8** **a** Correlation of annual mean surface pressure over the globe and the corresponding pressure at Darwin, Australia. **b** Spatial distribution of the strongest negative correlation at each grid point as taken from the corresponding one-point correlation map (see Wallace and Gutzler 1981). Correlations are based on months December–February) of the 200 model years 1901–2100, and consider only points north of 20°N. Contour interval is 20% with *shading* at intermediate values

ability in the climate system, at least some of which is expected to arise from coupled processes. (The comparison for JJA is not shown, but the discrepancies are similar). The observed estimate is based on only a 9 year period (1980–1988) from the ECMWF re-analysis (Gibson et al. 1997). Based on this rather limited data, Fig. 7 indicates that the model's spatial pattern of interannual variability is similar to that observed, but that the magnitude is underestimated in the extratropical winter storm track regions. This underestimate of extratropical variability appears to be a characteristic of the atmospheric component of CGCM1, as can be seen in the AMIP results described by D'Andrea et al. (1998).

Two other illustrations of variability in atmospheric circulation are shown in Fig. 8. Figure 8a shows the correlation of annual mean surface pressure at the model grid point nearest Darwin, Australia, with all other points on the globe in order to illustrate the shift in mass which accompanies ENSO events. A corresponding plot of this quantity, based on observations, is shown by Peixoto and Oort (1992), their Fig. 16.8 which is based on work of Trenberth and Shea (1987). The spatial pattern in the modelled version of this field is qualitatively very similar to that observed, for example the band of negative correlation in the eastern Pacific connected with the Southern Oscillation Index, and the low-high-low pattern from the north Pacific across North America and into the western mid-Atlantic which is reminiscent of the Pacific North America (PNA) pattern. The magnitude of the modelled correlations are, however, somewhat lower than observed in the extratropics, although the observations span only a 40 year period. Figure 8b shows the spatial distribution of the strongest negative correlation of DJF mean sea-level pressure at each point relative to all other points north of 20°N. The result can be compared to Fig. 16.15 in Peixoto and Oort (1992). The model result shows a robust and realistic North Atlantic Oscillation (NAO), but weaker correlations associated with the PNA and North Pacific Oscillation (NPO). More detailed analysis of hemispheric-scale modes of variability (Fyfe et al. 1999) indicates that the model produces realistic versions of the "Arctic and Antarctic Oscillations" and their correlations with surface temperature and zonal wind.

## 6.3 Precipitation and soil moisture

The hydrological cycle provides a direct connection between the atmosphere, ocean and land surface. Precipitation is, of course, an important component of the hydrological cycle and Fig. 9 compares the modelled mean DJF and JJA precipitation fields with the global

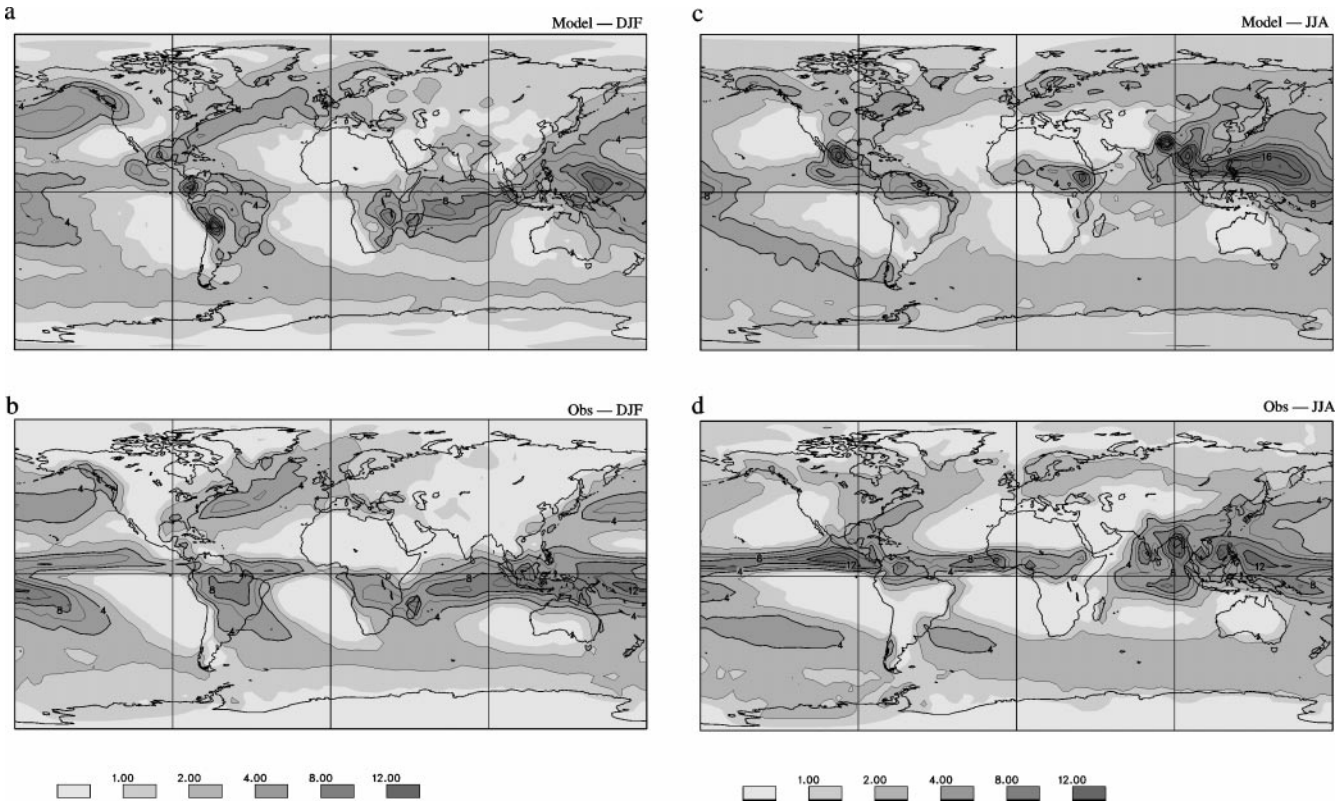


**Fig. 9** **a** Modelled mean DJF precipitation. **b** Observed DJF precipitation climatology (Xie and Arkin 1996, 1997). **c** As in **a** but for JJA. **d** as in **b** but for JJA. Contour interval is 2 mm/d

climatological estimates of Xie and Arkin (1996, 1997). Because of its high variability in both space and time, climatological estimates of precipitation are rather uncertain and so difference plots are not shown, however the model generally reproduces the observed global-scale spatial patterns in both seasons. As expected, these results differ little from those of MBBL, with rather excessive precipitation over high elevation regions, particularly in South America in DJF and the Himalayas in JJA, and too little precipitation in the tropics. The broad-scale features of the Asian monsoon are reproduced, although there are discrepancies in the detailed placement of precipitation maxima.

Variability of precipitation is illustrated in Fig. 10 which compares modelled and observed interannual standard deviation of DJF and JJA precipitation amounts. The observations, an extension of the data discussed by Hulme (1992, 1994), cover only a portion of the land-covered area for the period 1900–1995. As for temperature, a linear trend has first been removed prior to computing standard deviations. To the extent that the observations allow comparison in various geographical regions, the model does seem to realistically capture the magnitude and seasonal cycle of precipitation variability. A more quantitative comparison is provided by Tables 5 and 6 which show modelled and observed means and standard deviations (as before, differences not significant at the 5% level are shaded, and values in parentheses indicate model results obtained when using only the first 96 years of model output masked in such a way as to be consistent with the observations). The biggest differences are in the Sahel and South-east Asia in DJF, but in JJA, the model reproduces the mean and standard deviation of precipitation reasonably well.

### 6.4 Ocean structure and circulation

In this section we examine the ocean component of the model, beginning with the transport quantities shown in Table 2. Comparing results from the ocean-only spin-up to those for the coupled model illustrates that atmosphere/ocean interactions have substantially altered the ocean state. In particular, the Atlantic overturning circulation strengthens somewhat and with it, the northward transport of heat; although the heat transport remains below the observationally-based estimates. In the Pacific the heat transport and Indonesian throughflow are within the range of observational estimates, although at the low end. The Antarctic circumpolar circulation, represented by transport through Drake Passage, is apparently too weak in the spin-up, and decreases further upon coupling. Such changes presumably result from feedbacks and processes not included in the ocean-only spin-up. For example, the positive feedback between Greenland Sea ice edge retreat and enhanced

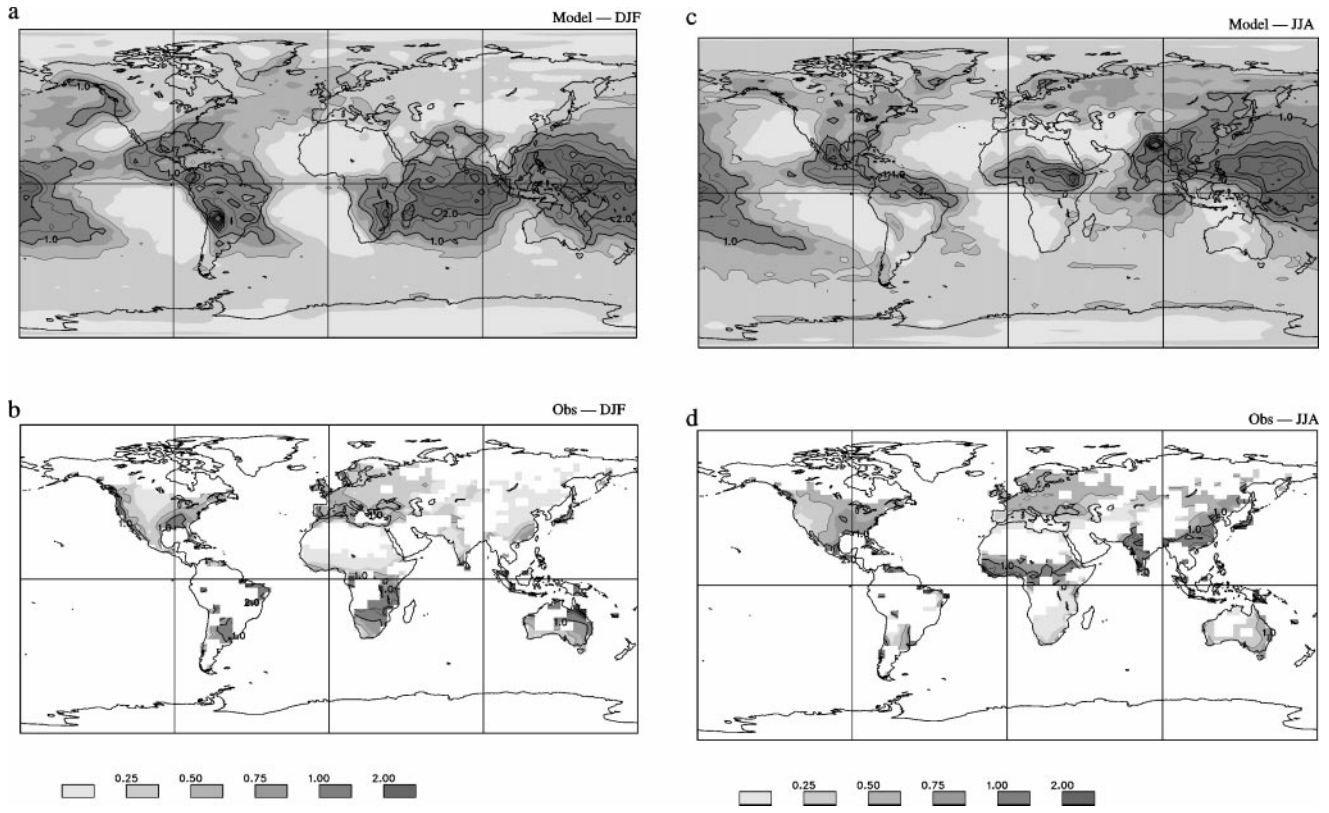


**Fig. 10a–d** Interannual standard deviation of seasonal mean precipitation. **a** Modelled, DJF. **b** Modelled, DJF. **c** Modelled, JJA. **d** Observed, JJA. Observations from Hulme (1992, 1994). Contour interval is 0.5 mm/d. Missing values in the observations have been masked

**Table 5** DJF land surface precipitation statistics

| Region[a] | Modelled mean (mm/d) | Observed mean (mm/d) | Modelled standard deviation (mm/d) | Observed standard deviation (mm/d) |
|---|---|---|---|---|
| NAM | 1.55 (1.54) | 1.35 | 0.20 (0.20) | 0.24 |
| SEA | 1.81 (1.81) | 0.68 | 0.34 (0.32) | 0.16 |
| SAH | 0.19 (0.23) | 0.05 | 0.04 (0.05) | 0.02 |
| SEU | 2.22 (2.23) | 1.84 | 0.20 (0.21) | 0.28 |
| AUS | 1.72 (1.79) | 2.69 | 0.37 (0.42) | 0.59 |

[a] See caption to Fig. 6 for definitions of the regions. Observations are from Hulme (1992, 1994) and cover the period 1900–1995. Values in parentheses indicate model results when only the first 96 years of output are used and masked in such a way as to be consistent with the observations. Shading indicates modelled and observed values whose difference is not statistically significant at the 5% confidence level (based on *t*- and *F*-tests for the mean and standard deviation respectively)

**Table 6** JJA land surface precipitation statistics

| Region | Modelled mean (mm/d) | Observed mean (mm/d) | Modelled standard deviation (mm/d) | Observed standard deviation (mm/d) |
|---|---|---|---|---|
| NAM | 3.41 (3.38) | 2.70 | 0.33 (0.30) | 0.34 |
| SEA | 8.88 (7.51) | 8.00 | 0.41 (0.49) | 0.51 |
| SAH | 3.39 (3.65) | 4.14 | 0.27 (0.32) | 0.49 |
| SEU | 1.41 (1.42) | 1.58 | 0.17 (0.18) | 0.19 |
| AUS | 0.81 (0.86) | 0.76 | 0.15 (0.15) | 0.22 |

high latitude heat loss to the atmosphere contributes to the increase in north Atlantic meridional overturning and the corresponding increase in northward heat transport (see Table 2). Likewise, strong feedbacks connecting sea-ice to deep convection in the Southern Ocean contribute to changes in deep water mass formation (as reflected in the reduction of AABW transport) and to corresponding changes in stratification (leading to a reduction in the strength of Antarctic circumpolar current via the joint effect of baroclinicity and relief).

Figure 11 shows the modelled ocean surface temperature (SST) for DJF and JJA (SST is defined here as the temperature of the uppermost ocean grid box, and so represents an average over the top 50 m of the ocean). Also shown in Fig. 11 is the difference between the modelled SST and the climatological estimate of Alexander and Mobely (1976), which was used in the initial ocean-only spin-up. The modelled surface temperatures agree with observations to within a degree over most of the tropical ocean, with errors increasing in the polar regions. The broad area of warming in the north Atlantic is consistent with the increase in meridional circulation and northward heat transport noted already.

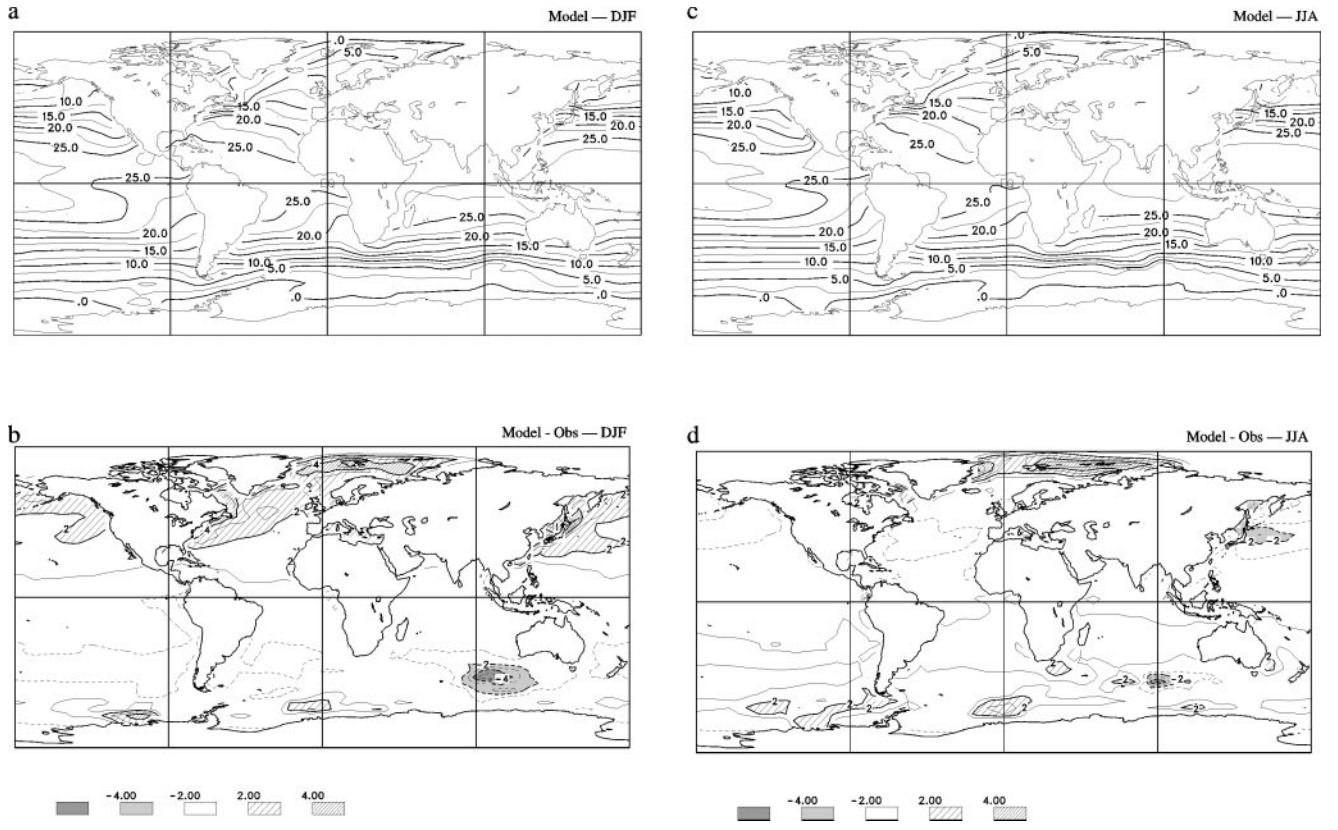


**Fig. 11** **a** Average DJF ocean surface temperature. **b** Difference between the modelled ocean surface temperature and DJF climatology (Alexander and Mobely 1976). **c** As in **a** but for JJA. **d** as in **b** but for JJA. Contour interval is 2.5 °C in parts **a** and **c**, and 1 °C in **b** and **d**. Positive errors are *hatched*, while negative errors are *shaded*

The modelled DJF and JJA ocean surface salinity fields are shown in Fig. 12, along with the differences from the Levitus et al. (1994) climatology. The errors have little seasonality and are confined primarily to the polar regions. The excess salinity in the Arctic arises from a small reduction in the net freshwater delivered by the atmosphere to the Arctic in the coupled model versus the uncoupled atmospheric spin-up. Because the Arctic is relatively isolated from the rest of the world ocean, a rather small bias in freshwater flux can lead to an increasing salinity error since there are no direct feedbacks to counteract it. The freshening around Antarctica is associated with a cessation of deep convection in these areas relative to the ocean spin-up, as will be seen in the following.

Zonal average plots of annual mean temperature and salinity are shown in Figs. 13 and 14, along with the differences from the Levitus and Boyer (1994) and Levitus et al. (1994) climatologies respectively. (Note that for presentation purposes, all the ocean fields have been averaged onto the lower-resolution AGCM grid). As is common in many models of this sort (e.g. Haidvogel and Bryan 1992), the ocean thermocline is excessively diffuse leading to deep ocean temperatures that are somewhat too warm and fresh. Such errors are reduced when more sophisticated mixing schemes are employed (e.g. McWilliams 1996). The differences in the high-latitude Southern Ocean, with anomalously cold surface temperatures underlain by anomalously warm temperatures, indicate increased stratification as a result of reduced deep convection (this can be seen in Fig. 14b which shows anomalously fresh water near the surface at high southern latitudes). Changes in convection patterns in this region after coupling have been demonstrated in simplified model by Lenderink and Haarsma (1994) and Rahmstorf (1995). These changes arise because the equilibrium obtained during the ocean spin-up may be unstable to perturbations in the strength of feedbacks at the surface. In the present case, coupling introduces strong positive feedbacks, such as the sea-ice albedo feedback, which were not present in the ocean spin-up. The result is a shift of convection from high southern latitudes to roughly 50–60°S (indicated by the salinity 'inversion' at this latitude in Fig. 14b). The rather large differences in both temperature and salinity just north of 60°N presumably result from misplacement of areas of deep convection in the Greenland and Norwegian Seas (and are exaggerated at this latitude of minimal ocean width).

The barotropic streamfunction is plotted in Fig. 15 showing that the strength of the midlatitude gyres are weak compared to observations, but similar to results

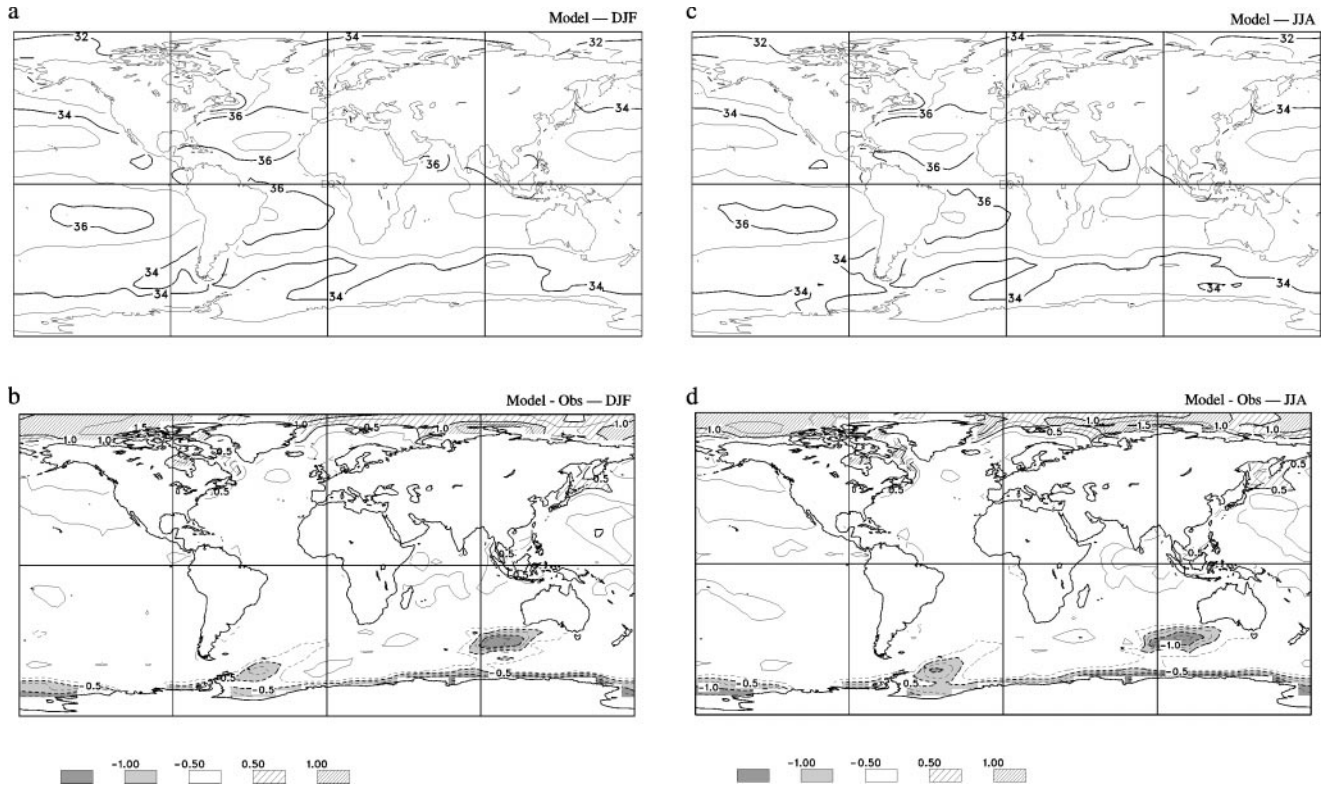


**Fig. 12** **a** Average DJF ocean surface salinity. **b** Difference between modelled DJF ocean surface salinity and climatology (Levitus 1982). **c** As in **a** but for JJA. **d** as in **b** but for JJA. Contour interval is 1PSU in parts **a** and **c**, and 0.25 PSU in **b** and **d**. Positive errors are *hatched*, while negative errors are *shaded*

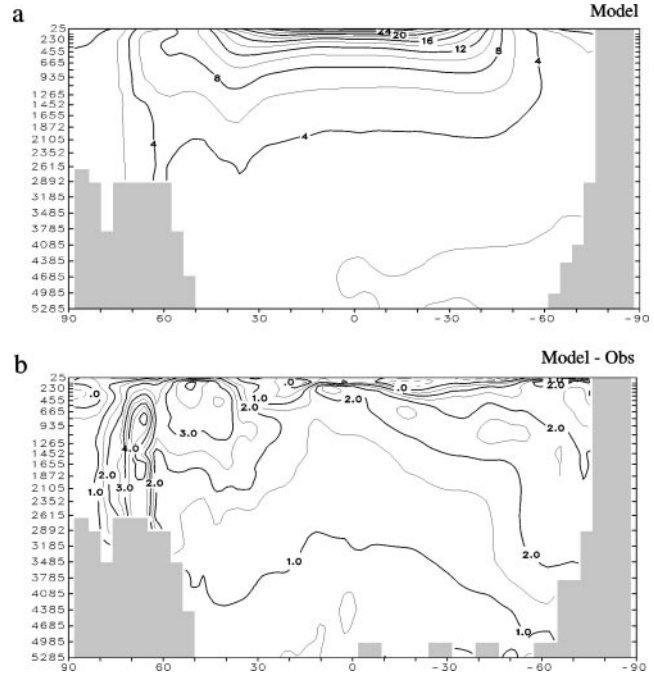


**Fig. 13** **a** Average annual modelled zonal mean ocean temperature. Contour interval is 2 °C. **b** Difference between modelled and observed (Levitus and Boyer 1994) zonal mean temperature. Contour interval is 0.5 °C

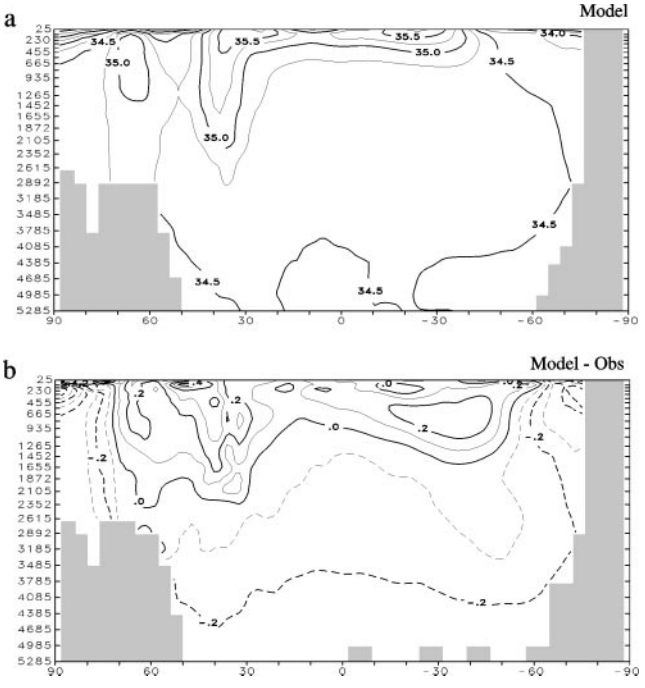


**Fig. 14** **a** Average annual modelled zonal mean ocean salinity. Contour interval is 0.25 PSU. **b** Difference between modelled and observed (Levitus et al. 1994) zonal mean salinity. Contour interval is 0.1 PSU

obtained by ocean models of this resolution. The strength of the Antarctic Circumpolar Current is weak compared to observationally based estimates (Read and Pollard 1993; see also Table 2). An illustration of the meridional circulation is provided by the annual mean north Atlantic overturning stream function in Fig. 16, along with a time series of its maximum value. (Note that the maximum is a point value from the full-resolution ocean data and so appears larger than the largest contour). The strength of the maximum overturning is somewhat higher than that obtained in other coupled models (e.g. the GFDL coupled model produces about 18 Sv, Delworth et al. 1993). A comparison of the modelled and observed maximum overturning stream function at 24°N is provided in Table 2, where again the model overturning appears to be somewhat strong. Irregular, interdecadal variability with a magnitude of about $\pm 2$ Sv is clearly evident in the bottom panel of Fig. 16. Although the amplitude is about the same, the time scale of this variability is somewhat shorter than the 50–60 year variations obtained by Delworth et al. (1993) in their model.

A final illustration of ocean variability is provided in Fig. 17 by the time series of the monthly SST anomaly in the NINO3 region of the tropical Pacific (indicated in Fig. 6). For comparison, the corresponding time series from the GISST2 historical SST reconstruction (Rayner et al. 1996), covering the period 1903–1995, is also shown and displays a remarkable increase in apparent variability during this period. The model exhibits considerably less variability than 'observed', showing no trend with time. This may be associated with the weaker than observed extratropical atmospheric variability noted earlier, as the atmospheric model produces a realistic extratropical response when forced with GISST temperatures.

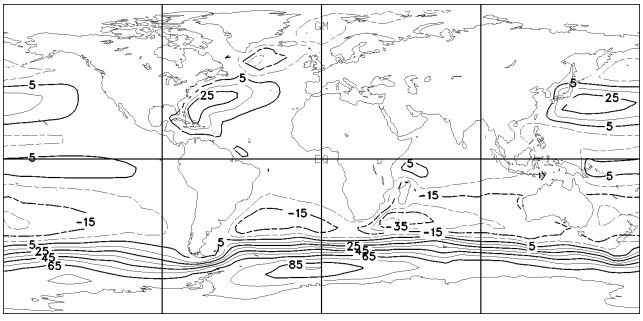

**Fig. 15** Modelled annual mean barotropic stream function in Sverdrups ($10^6$ m$^3$ s$^{-1}$)

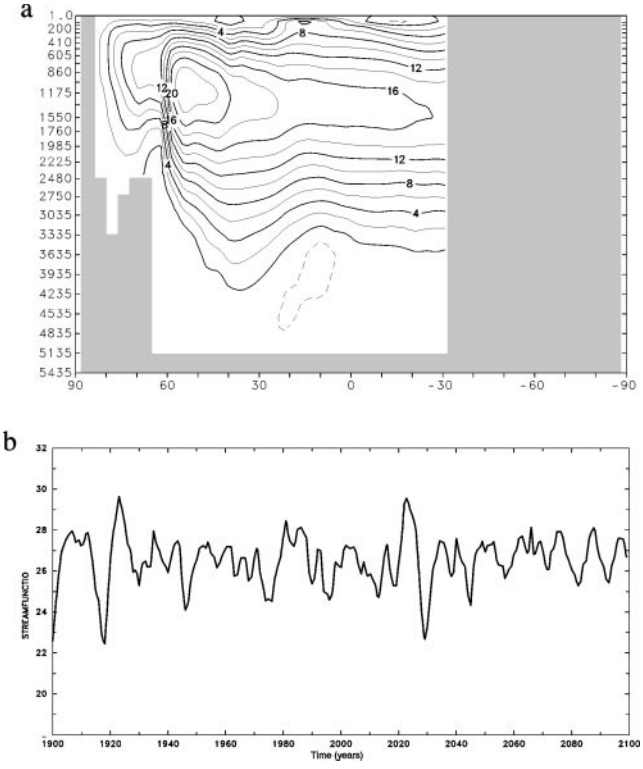


**Fig. 16** **a** Modelled annual mean meridional stream function in the Atlantic Ocean. Contour interval is 2 Sv. **b** Time series of maximum annual mean meridional stream function in the North Atlantic

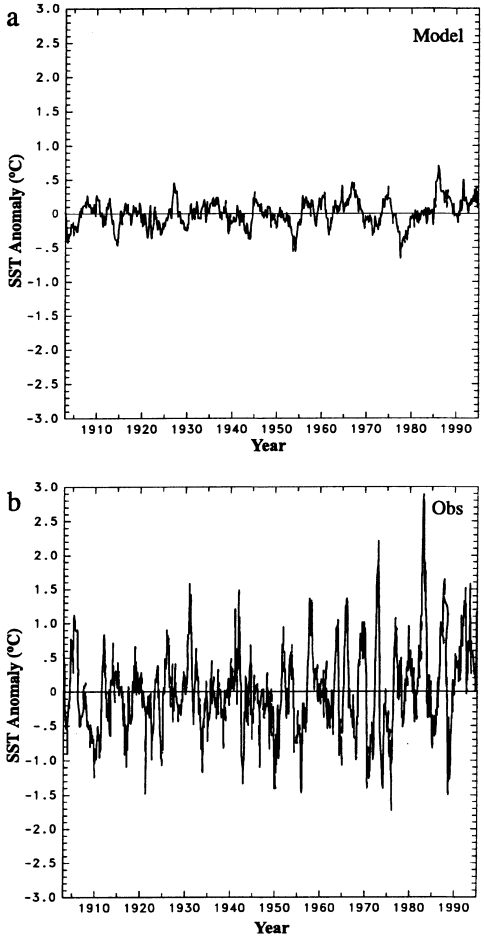


**Fig. 17a, b** Sea-surface temperature anomaly in the NINO3 region (see Fig. 6 for definition) from: **a** the model; **b** the GISST2 historical reconstruction (Rayner et al. 1996)

### 6.5 Cryosphere

The cryosphere in this model includes sea-ice, snow, and seasonally frozen soil moisture. Glaciers and ice sheets are represented as snow-covered land, with no explicit accounting of their mass balance (although the freshwater flux adjustment indirectly accounts for the return of water from the ice sheets to the ocean). The mean modelled ice thickness for March and September, the approximate times of maximum and minimum ice extent in both hemispheres, are shown in Fig. 18. Compared with observations like those of Gloersen et al. (1992), it is apparent that the ice extent is underestimated in the Northern Hemisphere in both seasons, whereas in the Southern Hemisphere, the ice extent is underestimated slightly in September and overestimated slightly in March. Quantitative comparisons are provided in Table 4. An illustration of the stability of the modelled ice cover is provided by Fig. 19 which shows the time series of March ice extent in the Northern Hemisphere and September ice extent in the Southern Hemisphere. In this figure the small trend toward de-

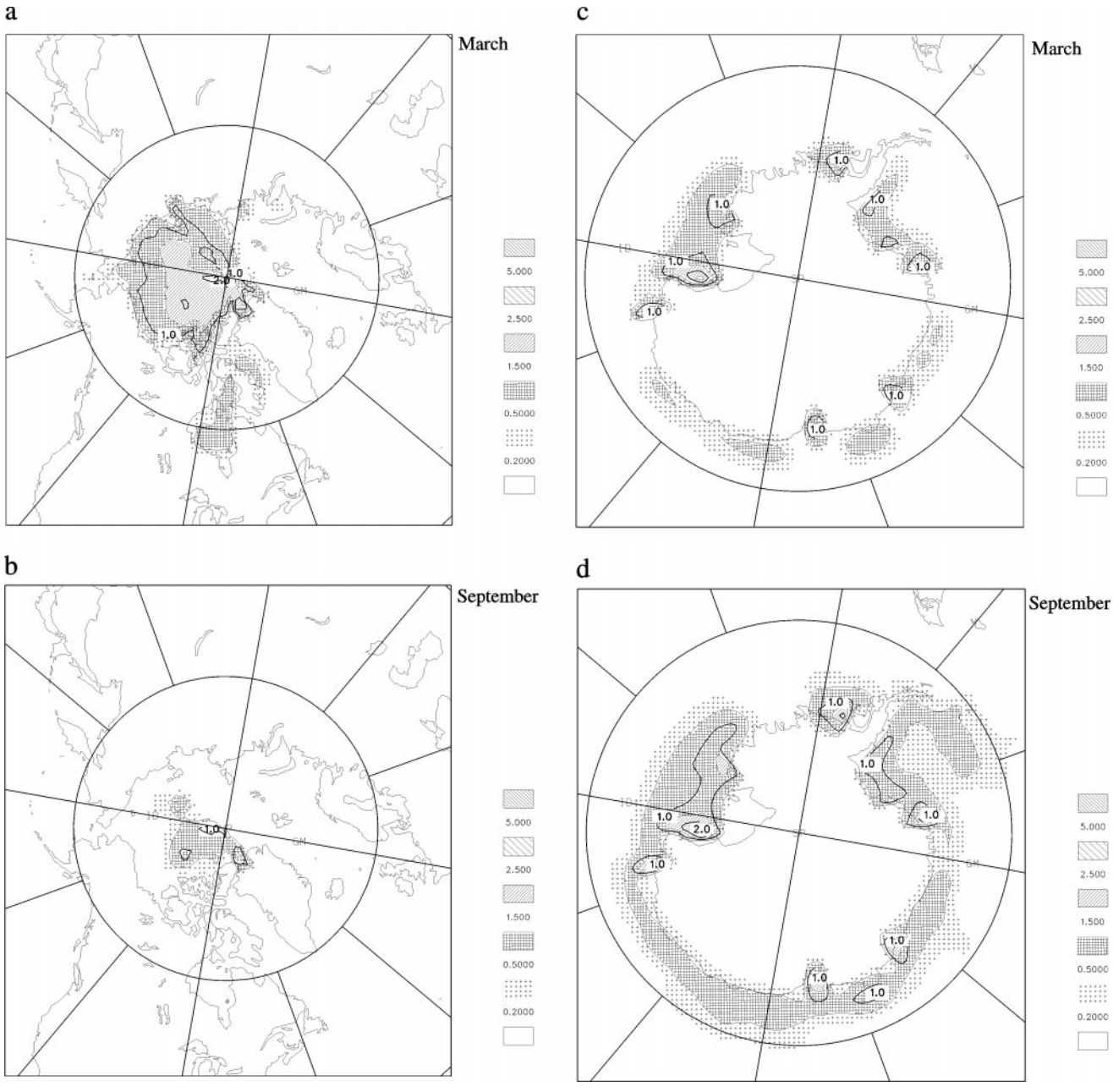


**Fig. 18a–d** Average modelled sea-ice thickness in the Northern Hemisphere, **a** March, **b** September; and in the Southern Hemisphere **c** March, **d** September. Thickness in meters

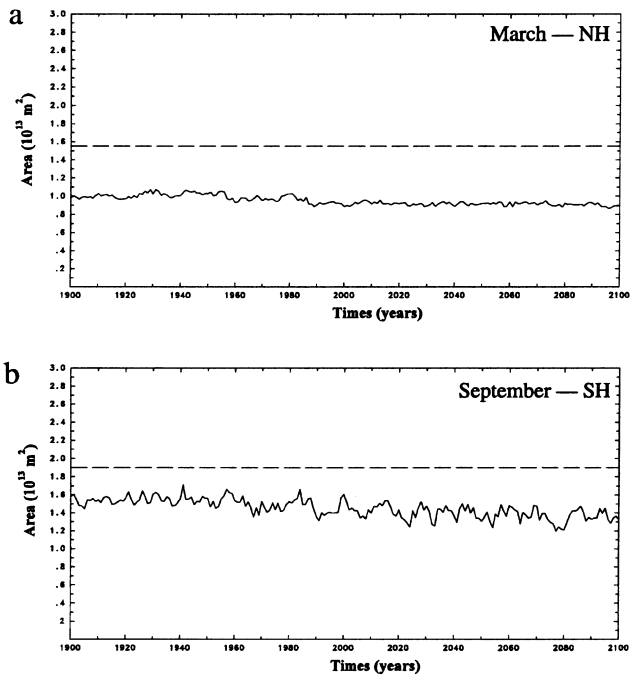


**Fig. 19a, b** Time series of modelled ice-covered area. **a** Northern Hemisphere, March. **b** Southern Hemisphere, September. *Dashed horizontal lines* indicate the 1978–87 observed average obtained by Gloersen et al. (1992) using passive microwave satellite data

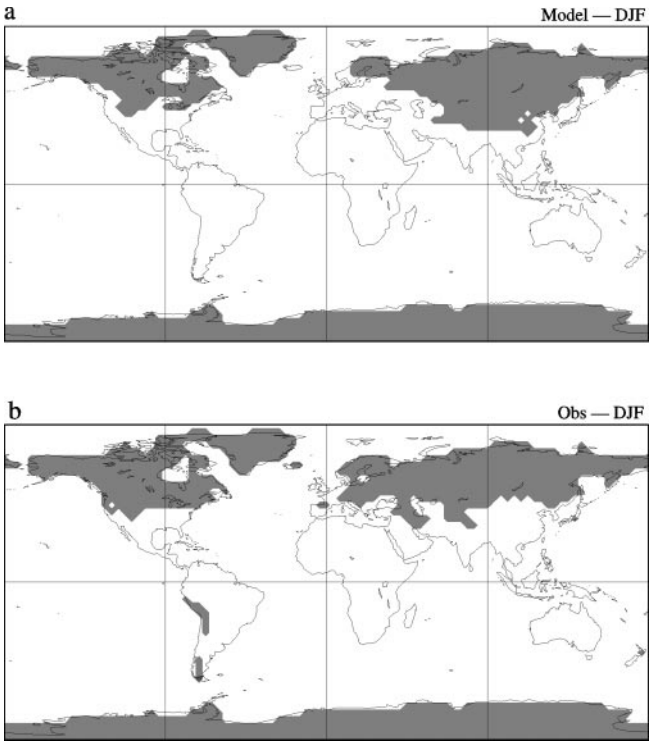


**Fig. 20a, b** DJF snow-covered land area. **a** Modelled. **b** Observed (Foster and Davy 1988). Land is considered snow-covered if snow amount exceeds 10 kg m$^{-2}$

creasing ice extent is visible in both hemispheres, as is the larger interannual variability in the Southern Hemisphere ice-covered area.

Modelled DJF snow-covered land area is shown in Fig. 20 along with a climatological estimate from Foster and Davy (1988). In both the model and observations, a land point is considered snow covered if the snow amount exceeds 10 kg m$^{-2}$. The model underestimates snow coverage in western Europe in this season, which is consistent with the warm bias noted in Table 3. On the other hand, the model overestimate snow coverage over the Mongolian Plateau, a discrepancy that has also been noted in other GCMs (e.g. Foster et al. 1996; Walland and Simmonds 1996). Both of these differences are likely related to the model's necessarily smooth representation of topography.

**Table 7** Ice extent statistics

| | Modelled mean (km$^2$) | Observed mean[a] (km$^2$) |
|---|---|---|
| NH, March | $9.6 \times 10^6$ | $15.5 \times 10^6$ |
| NH, September | $2.4 \times 10^6$ | $9 \times 10^6$ |
| SH, March | $6.6 \times 10^6$ | $4.5 \times 10^6$ |
| SH, September | $14.8 \times 10^6$ | $19 \times 10^6$ |

[a] Gloersen et al. (1992)

## 7 Discussion and conclusions

The Canadian global climate model extends the previous atmosphere/mixed-layer ocean model of McFarlane et al. (1992) to include the ocean's general circulation. The ocean component of the model is based on the widely-used GFDL MOM1 code, with a horizontal resolution of 1.86° and 29 vertical levels. As in other implementations of this code, horizontal viscosity and diffusivity coefficients are chosen on the basis of numerical stability. Vertical diffusivity is not strongly tied to numerical stability, and so we assess the effect of our particular choice through a series of ocean-only experiments. These indicate rather modest sensitivity of climatically important quantities like northward heat transport. Atmosphere-ocean coupling occurs daily and includes monthly flux adjustments for heat and freshwater, and a monthly ocean surface temperature adjustment. In this work, the model components and coupling scheme are described in detail, as is the spin-up and flux adjustment procedure.

In order to evaluate the coupled model, we perform a 200-year control simulation in which greenhouse gas concentrations are fixed at contemporary levels. Even with flux adjustment, the model exhibits a small secular climate drift of something less than 0.15 °C per century. This drift is associated with changes in feedback strength at the atmosphere/ice/ocean interfaces which arise upon coupling and are manifested by changes in ocean convection (and hence stratification) and an associated slow

recession of the polar sea-ice cover, particularly apparent in the northern north Atlantic.

The model's control climate is systematically compared with observations, both in terms of seasonal mean quantities and, when possible, interannual variability. We find that the model produces a realistic atmospheric climate in terms of global patterns of seasonal mean surface air temperature and precipitation, with local discrepancies tending to be largest in DJF and over land. The model also produces interannual variability of temperature and precipitation which agree well with observations, both in their broad features and in a more detailed comparison using the five regions identified in the 1990 IPCC report (Mitchell et al. 1990). This implies that internal processes in the modelled climate system, which give rise to such variability, are operating realistically, which in turn provides some confidence that the model will respond realistically to perturbations in external forcing. Modelled interannual variability in seasonal mean sea-level pressure tends to be low in the extratropical winter storm track regions, however the model does produce realistic-looking correlation patterns such as the NAO and PNA (although the latter tends to be slightly weak).

The modelled ocean provides a realistic simulation of surface temperature and salinity when compared to standard climatologies, with the largest discrepancies in the Arctic (mostly associated with the recession of sea-ice mentioned earlier). When compared to observational estimates, the model slightly underestimates the northward heat transport in both the Atlantic and Pacific at 24°N, but overestimates the north Atlantic overturning circulation. The modelled mass transport through the Indonesian Archipelago is within the range of observations, while the Antarctic circumpolar transport is less than observed. Comparison of modelled and observed surface temperature variability over the oceans indicate that the modelled ocean is rather more quiescent than is observed, particularly in the tropical Pacific. This may be due to unresolved boundary layer processes given that the ocean model's uppermost layer is 50 m thick.

Overall, the simulated climate agrees reasonably well with the observed contemporary climate of the Earth. The model is apparently operating in the same 'climate regime' as the present-day climate, and given its variability, has feedback processes which are likewise operating realistically. The model can therefore be used to conduct a suite of transient simulations, with increasing greenhouse gas and aerosol effects. These experiments are described in two companion papers (Boer et al. 2000a, b). The control climate described here provides the basis against which results of these perturbation experiments will be compared.

**Acknowledgements** We thank our colleagues at CCCma who have contributed to this effort in many ways. In particular, we thank Fouad Majaess, Bertrand Denis and Mike Lazare for assistance in computational matters, Steve Lambert for assistance with the observational data, and Peter Hollemans for assistance in constructing the runoff routing mask.

## References

Alexander RC, Mobley RL (1976) Monthly average sea surface temperatures and ice pack limits on a 1° global grid. Mon Weather Rev 104: 143–148

Boer GJ (1993) Climate change and the regulation of the surface moisture and energy budgets. Clim Dyn 8: 225–239

Boer GJ, McFarlane NA, Laprise R, Henderson JD, Blanchet J-P (1984) The Canadian Climate Centre spectral atmospheric general circulation model. Atmosphere Ocean 22(4): 397–429

Boer GJ, McFarlane NA, Lazare M (1992) Greenhouse gas-induced climate change simulated with the CCC second generation general circulation model. J Clim 5(10): 1045–1077

Boer GJ, Flato GM, Reader MC, Ramsden D (2000a) A transient climate change simulation with greenhouse gas and aerosol forcing: experimental design and comparison with the instrumental record for the 20th century. Clim Dyn 16: 405–425

Boer GJ, Flato GM, Ramsden D (2000b) A transient climate change simulation with greenhouse gas and aerosol forcing: projected climate change to the 21st century. Clim Dyn 16: 427–450

Bryan F (1987) Parameter sensitivity of primitive equation ocean general circulation models. J Phys Oceanogr 17: 970–985

Bryan K, Lewis LJ (1979) A water mass model of the world ocean. J Geophys Res 84: 2503–2517

Bryden HL, Roemmich DH, Church JA (1991) Ocean heat transport across 24°N in the Pacific. Deep-Sea Res 38: 297–324

Cummins PF (1991) The deep water stratification of ocean general circulation models. Atmos-Ocean 29: 563–575

D'Andrea F, and 16 others (1998) Northern Hemisphere atmospheric blocking as simulated by 15 atmospheric general circulation models in the period 1979–1988. Clim Dyn 14: 385–407

Delworth T, Manabe S, Stouffer RJ (1993) Interdecadal variations of the thermohaline circulation in a coupled ocean-atmosphere model. J Clim 6: 1993–2011

Fanning AF, Weaver AJ (1997) A horizontal resolution and parameter sensitivity study of heat transport in an idealized coupled climate model. J Clim 10: 2469–2478

Foster DJ Jr, Davy RD (1988) Global snow depth climatology. USAF publication USAFETAC/TN-88/006, Scott Air Force Base, Illinois, 48 pp

Foster J, Liston G, Koster R, Essery R, Behr H, Dumenil L, Verseghy D, Thompson S, Pollard D, Cohen J (1996) Snow cover and snow mass intercomparisons of general circulation models and remotely sensed datasets. J Clim 9: 409–426

Fouquart Y, Bonnel B (1980) Computation of solar heating of the Earth's atmosphere: a new parametrization. Beitr Phys 53: 35–62

Fyfe JC, Boer GJ, Flato GM (1999) The Arctic and Antarctic Oscillations and their projected changes under global warming. Geophys Res Lett 26: 1601–1604

Gates WL, Nelson AB (1975) A new (revised) tabulation of the Scripps topography on a 1° global grid. Part II: ocean depths. R-1227-1-ARPA, The RAND Corporation, Santa Monica, CA, 132 pp

Gates WL, Henderson-sellers A, Boer GJ, Folland CK, Kitoh A, McAvaney BJ, Semazzi F, Smith N, Weaver AJ, Zeng Q-C (1996) Climate models – evaluation. In: Houghton JT et al. (eds), Climate change 1995: the science of climate change. Cambridge University Press, Cambridge, UK, 572 pp

Gibson JK, Kallberg P, Uppala S, Hernandez A, Nomura A, Serrano E (1997) ECMWF reanalysis project Rep 1. ERA Description. ECMWF, Shinfield Park, UK

Gloersen P, Campbell WJ, Cavalieri DJ, Comiso JC, Parkinson CL, Zwally HJ (1992) Arctic and Antarctic sea ice, 1978–1987: satellite passive-microwave observations and analysis. NASA SP-511, National Aeronautics and Space Administration, Washington, 290 pp

Haidvogel DB, Bryan FO (1992) Ocean general circulation modelling, In: Trenberth KE (ed) Climate system modelling. Cambridge University Press, Cambridge, UK, pp 371–412

Hellerman S, Rosenstein M (1983) Normal monthly wind stress over the world ocean with error estimates. J Phys Oceanogr 13: 1093–1104

Hulme M (1992) Global land precipitation climatology for the evaluation of general circulation models. Clim Dyn 7: 57–72

Hulme M (1994) Validation of large-scale precipitation fields in general circulation models. In: Desbois M, Desalmand F (eds) Global precipitation and climate change. NATO ASI Series, Springer, Berlin, Heidelberg New York

Jenne RL (1975) Data sets for meteorological research. NCAR Tech Note, NCAR-TN/1A-111, NCAR, Boulder, 194 pp

Jones PD (1994) Hemispheric surface air temperature variations: a reanalysis and update to 1993. J Clim 7: 1794–1802

Killworth PD (1987) Topographic instabilities in level model OGCMs. Ocean Model 75: 9–12

Legates DR, Willmott CJ (1990) Mean seasonal and spatial variability in gauge-corrected global precipitation. Int J Climate 10: 111–127

Lenderink G, Haarsma RJ (1994) Variability and multiple equilibria of the thermohaline circulation, associated with deep water formation. J Phys Oceanogr 24: 1480–1493

Levitus S (1982) Climatological atlas of the world ocean. NOAA Prof Pap 13, US Department of Commerce, National Oceanic and Atmospheric Administration, Washington DC

Levitus S, Boyer TP (1994) World ocean atlas 1994 vol 4: temperature. NOAA Atlas NESDIS 4, US Department of Commerce, 117 pp

Levitus S, Burgett R, Boyer TP (1994) World ocean atlas 1994 vol 3: salinity. NOAA Atlas NESDIS 3, US Department of Commerce, 99 pp

Lukas R, Yamagata T, McCreary JP (1996) Pacific low-latitude western boundary currents and the Indonesian throughflow. J Geophys Res 101: 12 209–12 216

McFarlane NA, Boer GJ, Blanchet J-P, Lazare M (1992) The Canadian Climate Centre second-generation general circulation model and its equilibrium climate. J Clim 5(10): 1013–1044

McWilliams JC (1996) Modeling the oceanic general circulation. Ann Rev Fluid Mech 28: 215–248

Mitchell JFB, Manabe S, Meleshko V, Tokioka T (1990) Equilibrium climate change – and its implications for the future. In: Houghton JT et al. (eds) Climate change. Cambridge University Press, Cambridge, UK 365 pp

Morcrette J-J (1984) Sur la paraméterisation du rayonnement dans les modèles de la circulation générale atmosphérique. PhD thesis, l'Université des sciences et techniques de Lille, France, 373 pp

Nichols N, Gruza GV, Jouzel J, Karl TR, Ogallo LA, Parker DE (1996) Observed climate variability and change. In: Houghton JT et al. (eds) Climate change 1995: the IPCC second assessment. Cambridge University Press, Cambridge, pp 133–192

Parker DE, Folland CK, Jackson M (1995) Marine surface temperature: observed variations and data requirements. Clim Change 31: 559–600

Pacanowski RC, Dixon K, Rosati A (1993) The GFDL modular ocean model users guide. GFDL Ocean Group Tech Rep 2. Geophysical Fluid Dynamics Laboratory, Princeton, USA, 46 pp

Peixoto JP, Oort AH (1992) Physics of climate. American Institute of Physics, New York, 520 pp

Rahmstorf S (1995) Climate drift in an ocean model coupled to a simple, perfectly matched atmosphere. Clim Dyn 11: 447–458, 1995

Rayner NA, Horton EB, Parker DE, Folland CK, Hackett RB (1996) Version 2.2 of the global sea-ice and sea surface temperature data set, 1903–1994. Hadley Centre Climate Research Techn Note, CRTN 74, Sept., 1996, Hadley Centre, Meteorological Office, Bracknell, UK, 21 pp

Read JF, Pollard RT (1993) Structure and transport of the Antarctic circumpolar current and Agulhas return current at 40°E. J Geophys Res 98: 12 281–12 295

Sausen R, Barthel K, Hasselmann K (1988) Coupled ocean-atmosphere models with flux corrections. Czlim Dyn 2: 154–163

Schmitz WJ Jr, McCartney MS (1993) On the north Atlantic circulation. Rev Geophys 31: 29–49

Trenberth KE, Shea DJ (1987) On the evolution of the Southern Ocean. Mon Weather Rev 115: 3078–3096

Wallace JM, Gutzler DS (1981) Teleconnections in the geopotential height field during the Northern Hemisphere winter. Mon Weather Rev 109: 784–812

Walland DJ, Simmonds I (1996) Sub-grid-scale topography and the simulation of northern hemisphere snow cover. Int J Climatol 16: 961–982

Weaver AJ, Hughes TMC (1996) On the incompatibility of ocean and atmosphere models and the need for flux adjustments. Clim Dyn 13: 141–170

Xie P, Arkin A (1996) Analyses of global monthly precipitation using gauge observations, satellite estimates and numerical model predictions. J Clim 9: 840–858

Xie P, Arkin A (1997) Global precipitation: a 17-year monthly analysis based on gauge observations, satellite estimates and numerical model outputs. Bull Am Meteoral Soc 78(11): 2539–2558